

Communication

Effect of Operating Temperature on Individual Half-Cell Reactions in All-Vanadium Redox Flow Batteries

Ruediger Schweiss * , Christian Meiser and Dana Dan

SGL Carbon GmbH, Werner-von-Siemens-Straße 18, D-86405 Meitingen, Germany;
christian.meiser@sglcarbon.com (C.M.); dana.cazimir@sglcarbon.com (D.D.)

* Correspondence: ruediger.schweiss@sglcarbon.com; Tel.: +49-8271-83-1702

Received: 26 September 2018; Accepted: 30 October 2018; Published: 1 November 2018



Abstract: Systematic steady-state measurements were performed in order to investigate the effect of operating temperature on the individual half-cell reactions in all vanadium redox flow cells. Results confirm that the kinetic losses are dominated by the negative half-cell reaction. Steady-state polarization and AC impedance measurements allowed for extraction of kinetic parameters (exchange current densities, activation energy) of the corresponding half-cell reaction.

Keywords: vanadium redox flow batteries; operating temperature; electrocatalysis; kinetics; electrodes

1. Introduction

Redox flow battery technology lends itself to large-scale storage of energy harvested from intermittent sources such as wind or solar power [1–4]. The appeal of this technology is related to its prospects of a high degree of modularity, fast response time, inherent safety and prolonged cycle life [5–7]. Despite the multitude of different chemistries proposed in recent years [8], by far the dominant type used in commercial systems is the all-vanadium redox flow battery (VRFB) already introduced by M. Skyllas-Kazacos in the 1980s [9,10]. The well-founded advantage of the VRFB lies in the use of different redox states of a single element species to drive both half-cell reactions. As a consequence, capacity losses caused by the undesired crossover of active materials can be conveniently regenerated in a subsequent charge/discharge cycle. On the other hand, some of the vanadium species involved suffer from limited solubility, thus restricting energy density. Another concern is related to the precipitation of high valence vanadium oxides (mostly V_2O_5), which becomes progressively problematic at operating temperatures above 40 °C in common VRFB electrolytes [11].

Notwithstanding the above, VRFB has attained the highest degree of technical and commercial maturity of all flow battery types. For a large part, this preeminence has been nurtured by a wealth of research and development activities carried out with respect to improved vanadium electrolytes [11,12], ion-exchange membranes with both high conductivity and selectivity [13,14], more efficient electrodes [15], as well as on a wide spectrum of theoretical approaches [16–19] to understand the rather complex interactions which govern the performance and lifetime of VRFBs.

Temperature plays a pivotal role with respect to the stability of the vanadium electrolyte. Hence, the main effort has been focused on developing more concentrated vanadium electrolytes which facilitate VRFB operation within a larger temperature window [20]. In terms of the effects of cell temperature on electrochemical processes in VRFBs, scholarly references are relatively scarce. As expected, model studies on graphite electrodes show more favorable kinetics at an elevated temperature for the positive redox couple [21]. Langner et al. [22] studied the electrochemistry of the negative redox couple (V^{2+}/V^{3+}) at more practically relevant (carbon felt) electrodes by means of cyclic

voltammetry. They found indications that parasitic side reactions such as hydrogen evolution might become increasingly problematic at elevated temperatures. Similar observations were made in actual cells using reference electrodes to monitor the overpotentials [23] or by visualization of the formed hydrogen bubbles in transparent cells [24]. Single cell studies revealed a $90 \text{ mW}\cdot\text{cm}^{-2}$ peak power gain by increasing the operating temperature from $15 \text{ }^\circ\text{C}$ to $55 \text{ }^\circ\text{C}$ [25]. This gain in power density, however, was almost nullified by lower coulombic efficiency and a rapid drop in capacity. Xi et al. [26,27] studied single cells from $-20 \text{ }^\circ\text{C}$ up to $50 \text{ }^\circ\text{C}$. They found almost constant voltage efficiency from 30°C to 50°C , while the coulombic efficiency steadily decreased with increasing cell temperature due to vanadium crossover. Overall, an operating temperature of $40 \text{ }^\circ\text{C}$ has been suggested for optimum electrolyte utilization. Finally, modelling studies have been performed to predict the evolution of cell temperature depending on components and operational parameters [28].

To arrive at a more detailed understanding of the impact of temperature on VRFB performance, knowledge of the temperature effect on the individual half-cells is a crucial aspect—particularly because the redox chemistry of both half-cell couples is significantly different. For instance, the $\text{V}^{2+}/\text{V}^{3+}$ redox couple (negative) is known as a typical inner-sphere redox system which has rather poor kinetics on carbon and which is inherently sensitive to surface oxygen groups on the carbon fibers. Moreover, the negative half-cell reaction is affected by parasitic side reactions such as hydrogen formation [23,29]. Consequently, Bourke et al. [30] found substantial differences in the kinetics of the negative electrode depending on oxidative or reductive pretreatment. Previous studies in our lab confirmed correlations between the number of surface oxygen groups (e.g., $-\text{C}=\text{O}$) and the kinetics (exchange current densities normalized to the BET surface area) of the negative couple [31]. By contrast, the redox chemistry of V(IV) and V(V) species is very complex (i.e., multistep reaction pathways) [32] and displays a dependence of the reactivity on the graphitic character of the carbon electrode [31,33]. This study investigates the effects of the operating temperature on the individual half-cell reactions by means of steady-state (double half-cell) measurements [31,34,35] with both redox couples. Experiments were carried out in each case with two Nafion[®] membranes (Ion Power, Munich, Germany) with the same properties but different thickness in order to quantify the membrane contributions.

2. Results

2.1. Full Cell Test

Figure 1 shows the typical performance parameters of a full cell at three different temperatures.

The observed trends corroborate the findings of previous studies. The increase in voltage efficiency in line with temperature can be attributed to better ionic conductance (porous electrode and membranes) as well as to faster charge-transfer kinetics. This beneficial trend comes at the expense of a lower current efficiency at elevated temperature, which is a result of an increased crossover of vanadium species [25]. The cell temperature of $35 \text{ }^\circ\text{C}$ yielded the best compromise between voltage and current efficiency (product of both yields the highest value). The observed effects on voltage and coulombic efficiency were very similar to studies using other types of membranes [25,26,36]. In the main part of this study, we present a methodology to break down the temperature effects on the corresponding half cells.

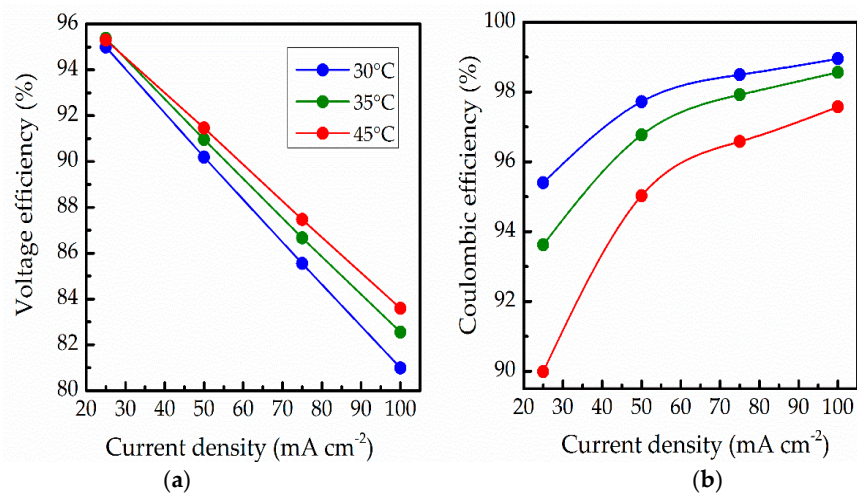


Figure 1. Voltage efficiency (a), coulombic efficiency (b) of VRFB single cells with 20 cm² active area at 30, 35 and 45 °C. Cycling was performed using a Fumasep[®] FAP450 anion-exchange membrane and with a 1.6 M Vanadium electrolyte between state-of-charge (SOC) of 10% and 90%.

2.2. Effects on Porous Electrode

As the porous electrode constitutes a mixed conductor (electronic and ionic transport), the resistance is determined by the electronic conductivity of the fibrous skeleton (σ_s) and the ionic conductivity within its voids (κ_L). The latter was calculated based on the measured bulk conductivity of the vanadium electrolyte (κ_V) and the porosity of the compressed felt (ϵ_c) using a Bruggeman approximation [19].

$$\kappa_L = \kappa_V \cdot (\epsilon_c)^{1.5} \quad (1)$$

Figure 2a shows the area-specific ionic resistance (L/κ_L) calculated based on electrolyte conductivities (κ_V), Figure 2b) measured at different temperatures (L is the thickness of the porous electrode). As expected, the ionic conductivity of the porous electrode is more than one order of magnitude lower than its electronic conductance (σ_s) and increases with temperature. The total Ohmic resistance (R_e^Ω) of the porous electrode is then given by a parallel combination of two resistors (L/σ_s and L/κ_L).

$$R_e^\Omega = \frac{L}{\sigma_s + \kappa_L} \quad (2)$$

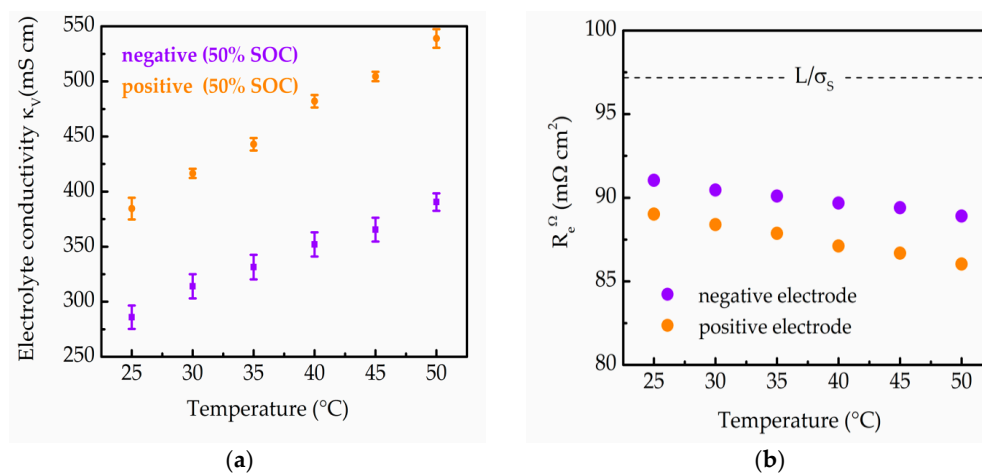


Figure 2. (a) Measured electrolyte conductivities (κ_V) and (b) calculated total Ohmic electrode resistances (R_e^Ω) for negative and positive electrolytes/electrodes at temperatures from 25 to 50 °C.

Figure 2 shows the measured electrolyte conductivities and the calculated ohmic resistances (Equation (2)) of the porous electrodes at different temperatures.

As expected, the conductivities of both half-cell electrolytes increase with temperature as shown in previous studies [37].

2.3. Double Half-Cell Measurements

In order to assess the charge transfer kinetics, we applied the method of double half-cell measurements (DHC) recently introduced by Darling and Perry [34,35]. This simple method features the same electrolyte composition in both half cells (either V^{2+}/V^{3+} or VO^{2+}/VO_2^+), meaning that it mimics a vanadium redox flow battery which is at steady-state conditions (i.e., operating at constant state of charge). Such measurements are particularly useful since concentration polarization is negligible, and due to the use of the same redox species on both electrodes, the dissection of the voltage losses is vastly simplified. Additionally, potential crossover of species does not lead to a distortion of the electrode performance parameters, which occurs in cycling studies on full cells. In our previous work, we have successfully employed this method to study different carbon felt type electrodes with respect to their catalytic activity for both half-cell reactions [31].

Upon passing a current (i_{app}) through such a cell, the potential of the double-half cell (E_{DHC}) with a geometric area A_e is given by

$$E_{DHC} = \frac{i_{app}}{A_e} \cdot R_{DHC} \quad (3)$$

R_{DHC} contains contributions from the resistance of the ion-exchange membrane (R_m), the contact and collector resistances (R_{cc}) and the resistance of the porous electrodes (R_e)

$$R_{DHC} = 2R_e + R_m + 2R_{cc} \quad (4)$$

R_e comprises Ohmic resistances and overpotentials associated with charge-transfer kinetics. The high-frequency impedance (Z_{DHC}^{HF}), which is typically taken from the impedance spectra section where AC voltages and currents are in phase at high frequencies (HF), yields the purely conductive (Ohmic) losses of the cell [38]

$$Z_{DHC}^{HF} = 2 \cdot R_e^\Omega + R_m + 2R_{cc} \quad (5)$$

In accordance with the widely-known 1D porous electrode model developed by Newman [39], the total resistance of either electrode (R_e), which contains Ohmic and kinetic elements, can be approximated by

$$R_e = R_e^\Omega \cdot \left[1 + \frac{2 + \left(\frac{\sigma_s}{\kappa_L} + \frac{\kappa_L}{\sigma_s} \right) \cdot \cosh(y)}{y \cdot \sinh(y)} \right] \quad (6)$$

with y being a dimensionless quantity describing the rate of charge transfer

$$y = \sqrt{j_0 S_a \cdot \frac{FL^2}{RT} \left(\frac{1}{\kappa_L} + \frac{1}{\sigma_s} \right)} \quad (7)$$

Equation (6) holds for linear polarization, a condition which applies to DHCs. As it is rather difficult to determine the (active) surface area (S_a) of the porous electrode accurately [40,41], the volumetric exchange current density ($j_0 \cdot S_a$) [38] is used as a quantity describing the charge-transfer kinetics (S_a values of virgin carbon felts are typically around 500 cm^{-1}). Fitting the experimentally

accessible values of double-half cell resistance (R_{DHC}) and high-frequency impedance ($Z_{\text{DHC}}^{\text{HF}}$) to Equation (8) allows for the calculation of kinetic parameters (y).

$$R_{\text{DHC}} - Z_{\text{DHC}}^{\text{HF}} = 2R_e^{\Omega} \cdot \left[\frac{2 + \left(\frac{\sigma_s}{\kappa_L} + \frac{\kappa_L}{\sigma_s} \right) \cdot \cosh(y)}{y \cdot \sinh(y)} \right] \quad (8)$$

Figure 3 shows the polarization curves of negative and positive double half-cells using Nafion[®] NR-211 and NR-212 ion exchange membranes. As expected, the positive double-half cells show a significantly lower DHC resistance due to the higher conductivity of the positive electrolyte and the faster kinetics of the positive couple. This is highly consistent with previous studies [29,41–43]. Similarly, a clear distinction between DHCs built using NR-211 and NR-212 membranes is observed.

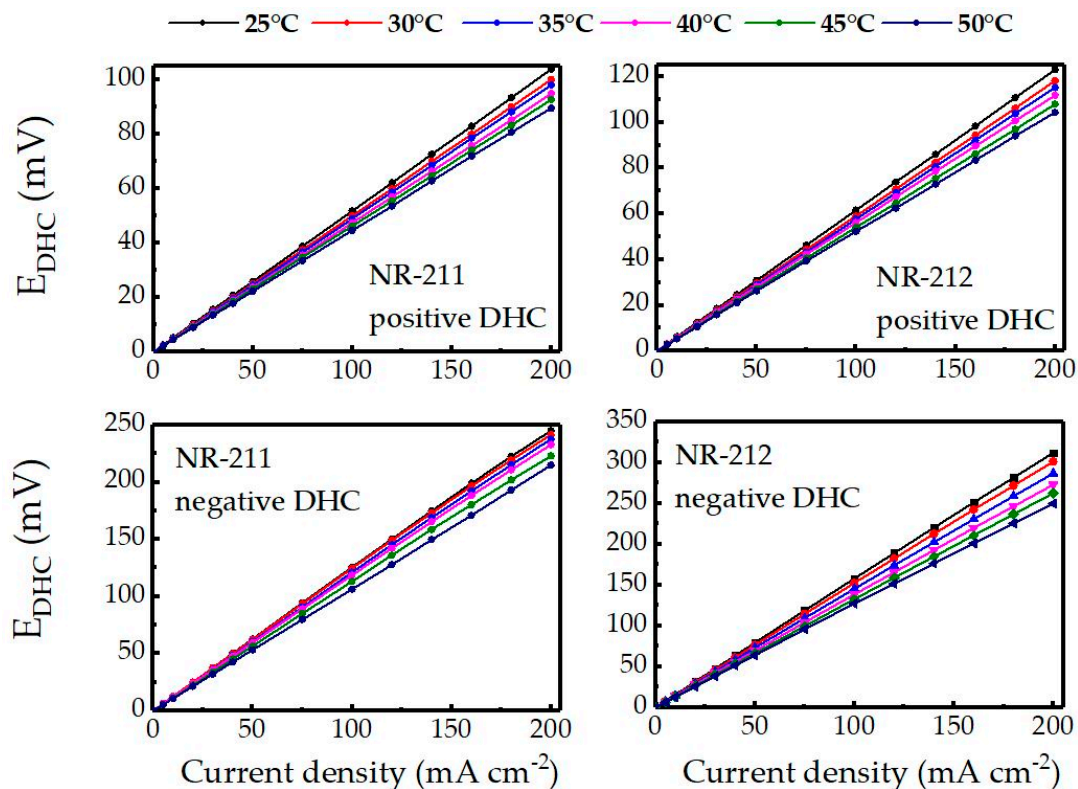


Figure 3. Double half-cell measurements (DHC) polarization curves using positive and negative electrolytes (1.6 M vanadium, both at SOC = 50%) and Nafion[®] NR-211 and NR-211 membranes at operating temperatures ranging from 25 °C to 50 °C.

The difference in DHC resistance can be used in order to quantify the effect of the membrane on the DHC resistance (see Supplementary Figure S1), since the specific conductivities of both membranes can be assumed to be identical. Taking the average value of the difference between positive and negative DHCs, we can estimate, for a full cell at SOC = 50%, an area-specific resistance (ASR) of a Nafion[®] NR-212 of 321 $\text{m}\Omega \cdot \text{cm}^2$ (30 °C) and 252 $\text{m}\Omega \cdot \text{cm}^2$ (50 °C). These values are consistent with values reported in the literature [44,45]. Fitting the experimentally determined resistance and impedance values (Figure 4a) and material parameters (κ_V , σ_S , ϵ) to Equation (8), the volumetric exchange current densities ($j_0 \cdot S_a$) could be obtained for both half-cell reactions (Figure 4b).

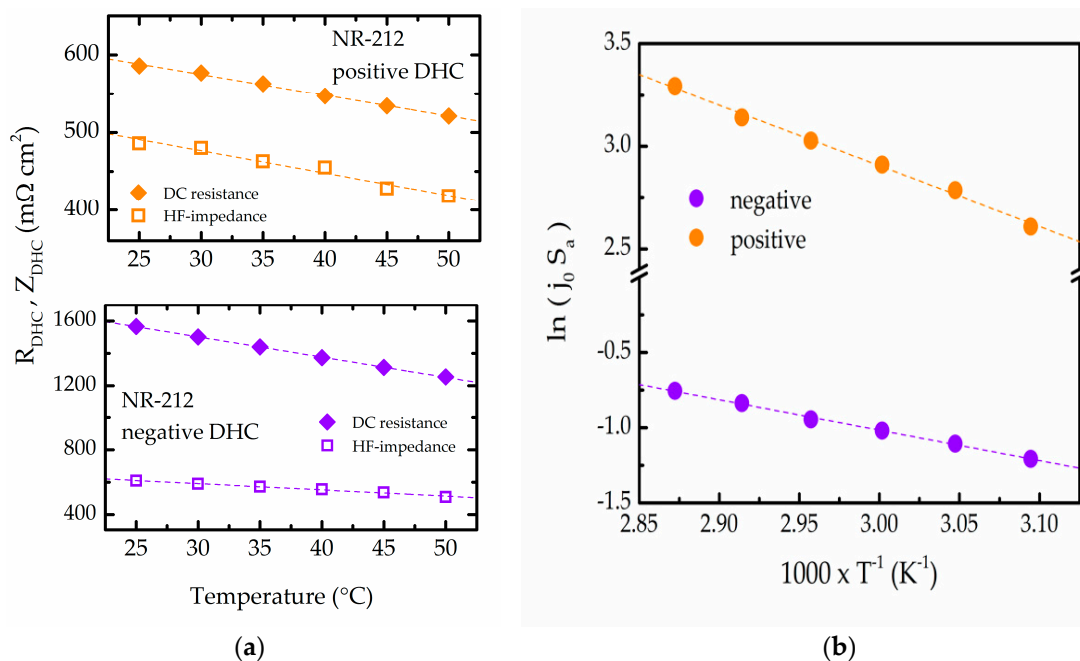


Figure 4. (a) Positive and negative DHC resistances (R) and high-frequency impedances (Z) for a cell using Nafion[®] NR-212 membranes at different temperatures. (b) Calculated volumetric exchange current densities (natural logarithm) for both half-cell reactions at different temperatures.

Volumetric exchange current densities ($j_0 \cdot S_a$) of negative and positive couples differ by almost two orders of magnitude (ratio positive to negative of between 40 and 51 depending on the temperature). A similar ratio has been observed in previous investigations, which performed a deconvolution of voltage losses by means of single-electrode impedance spectroscopy and reference electrodes [42,43]. For the sake of comparison with previous studies based on different methodologies, we estimated S_a by multiplying the BET surface area of the felt ($3.8 \text{ m}^2 \text{ g}^{-1}$) by its bulk density (0.09 g cm^{-3}). This yields exchange current densities related to the geometric area of between 0.09 and $0.14 \text{ mA cm}^{-2}_{\text{geo}}$ for the negative and between 3.5 and $7.7 \text{ mA cm}^{-2}_{\text{geo}}$ for the positive couple. These values are highly consistent with previous findings, which report $0.15/4.3 \text{ mA cm}^{-2}_{\text{geo}}$ and $0.149/6.65 \text{ mA cm}^{-2}_{\text{geo}}$ (ratio of positive to negative of 44) [46]. As the temperature dependence follows an Arrhenius-type behaviour for both redox couples, the activation energy ΔH^\ddagger can readily be obtained by differentiation

$$\frac{d \ln(j_0 \cdot S_a)}{dT^{-1}} = -\frac{\Delta H^\ddagger}{R} \quad (9)$$

The values found ($18.5 \text{ kJ} \cdot \text{Mol}^{-1}$ for $\text{V}^{2+}/\text{V}^{3+}$ and $24.6 \text{ kJ} \cdot \text{Mol}^{-1}$ for $\text{VO}^{2+}/\text{VO}_2^+$) are comparable to values gained from impedance analysis (charge-transfer resistance) of single electrodes [37].

3. Discussion

The effect of operating temperature on both half-cell reactions in vanadium redox flow batteries was studied by means of steady-state measurements. This methodology facilitates the evaluation of the temperature effect on the individual redox reactions in VRFBs. It has been confirmed that, even for surface-treated electrodes, the rate of charge-transfer of the negative half-cell reactions are around 50 times lower than those for the positive half-cell. Both half-cells showed a linear increase in the rate of charge transfer with cell temperature, which allows for the calculation of the activation energy. The latter was on a similar level for both redox couples. Taking the temperature dependence of the voltage losses associated with both half-cells from this study we can make simple estimations on the effect of full cell resistance. For a VRFB cell with a Nafion[®] N212 membrane this amounts to a drop in

cell resistance of $78 \text{ m}\Omega\cdot\text{cm}^2$ per 10 K temperature increase. This value is comparable to the actual full cell data obtained using Fumasep[®] membranes (Figure 1a), for which a temperature increment of 10 K produced a reduction in cell resistance of $87 \text{ m}\Omega\cdot\text{cm}^2$.

Our current efforts extend this approach to the study of ageing of carbon felt electrodes in vanadium redox flow batteries.

4. Materials and Methods

All cells were built using commercially available materials. Surface-treated SIGRACELL[®] GFD 4.6 carbon felts (SGL Carbon, Meitingen, Germany) were used as electrode materials as described in Reference [29]. Glassy carbon (Sigradur[®], HTW, Thierhaupten, Germany, 2 mm) was chosen as the plate material for the full cell test as it is more stable at high SOC than graphite (which is prone to exfoliation). Full cell tests were carried out with an anion-exchange membrane (Fumasep[®] FAP450, Fumatech, Bietigheim, Germany). A commercial vanadium electrolyte (1.6 M vanadium in 2 M sulfuric acid, GFE, Nuremberg, Germany) was used in all tests. Prior to DHC measurements, negative and positive electrolytes were adjusted to a state of charge (SOC) of 50% in a separate full cell. The SOC of the electrolytes was validated by measurements using a glassy carbon electrode against a saturated mercury sulfate reference electrode (SMSE, $E_0 = +0.658 \text{ V}$) prior to DHC tests. All experiments were conducted using homebuilt cells with active areas of 20 cm^2 . The cells were assembled applying a felt compression to $75 \pm 1\%$ with respect to the uncompressed thickness (4.7 mm, L_0). L refers to the actual thickness of the porous electrode (distance from the separator to the current collector). The porosity of the electrode (ϵ) results as follows

$$\epsilon = 1 - (1 - \epsilon_0) \cdot \frac{L_0}{L} = 1 - \frac{(1 - \epsilon_0)}{0.75} \quad (10)$$

With a porosity of the uncompressed felt (ϵ_0) of 0.945 (determined by mercury intrusion), we obtained a felt of 0.927 for the compressed electrode (ϵ). Full cell tests were performed using charge-discharge cycles at current densities with the end of charge/discharge being controlled by means of an open-circuit voltage (OCV) cell which was put in in series with the operating cell as described previously. For the OCV, a temperature coefficient of $1.6 \text{ mV}\cdot\text{K}^{-1}$, which is consistent with published values and our own calibration measurements, was used. Galvanostatic charge-discharge cycling tests were performed between 10% and 90% SOC. Electrolyte circulation was maintained by two Liquiport[®] diaphragm pumps (KNF Neuberger, Freiburg, Germany) operating at flow rates of 90 mL min^{-1} . A modified Scribner 857 flow battery test setup (Northern Pines, NC, USA) was used to record the current-voltage curves. The temperature was controlled by putting both electrolyte tanks in a thermostat bath. For double half-cells (DHCs), two cation exchange membranes (Nafion[®] NR-211 and NR-212, Ion Power, Munich, Germany) were used. SIGRACELL[®] TF6 flexible graphite plates (0.6 mm, SGL Technik, Valencia, CA, USA) served as current collectors in double half-cell measurements. Polished 2 mm copper plates, which served as current collector terminals, were each equipped with two screw contacts and leads (voltage and current).

The conductivity of the electrolyte was monitored during the tests (Mettler Toledo, Urdorf, Switzerland). Impedance spectra (amplitude 10 mV rms, 0.1 Hz to 100 KHz) were recorded at open-circuit potential before and after measurement of the polarization curves by means of a Solartron 1270/1260 potentiostat/frequency response analyzer. Measurements were carried out using Nafion[®] NR-211 (dry thickness 25 μm) and Nafion[®] NR-212 (dry thickness 51 μm), respectively. The membranes were equilibrated using alternating constant current cycling for 10 min. The area-specific electronic resistance of the porous electrode (L/σ_s) was obtained from two-point measurements with gold-plated contacts. R_{cc} was determined to $30 \pm 5 \text{ m}\Omega\cdot\text{cm}^2$ using plate/felt sandwiches with 4 different felts (variable thickness but identical porosity) and extrapolation to zero felt thickness [47]. Complementary measurements with a 'dry' cell (VRFB cell assembled without membrane) using the same felt compression level showed that the R_{cc} values are consistent.

Supplementary Materials: The following are available online at <http://www.mdpi.com/2313-0105/4/4/55/s1>, Figure S1: Difference in resistance of positive and negative DHCs using NR-211 and NR-212 membranes at different temperatures.

Author Contributions: Conceptualization, visualization, validation, manuscript writing, R.S.; Cell building and data acquisition, C.M. and D.D.; Test bench maintenance, C.M.

Acknowledgments: The authors thank Swati Poduval (now at Konrad Technologies, Germany) for coding a tailor-made routine for controlling the test benches and for data processing.

Conflicts of Interest: The authors declare no conflict of interest.

Nomenclature

List of symbols and acronyms.

Symbol	Denotation	Unit
A_e	Electrode area (2D)	cm^2
BET	BET surface area	$\text{m}^2 \text{g}^{-1}$
E_{DHC}	Double-half cell potential	mV
ΔH^\ddagger	Activation enthalpy	kJ Mol^{-1}
ϵ_0	Porosity of the uncompressed felt	-
ϵ	Porosity of the uncompressed felt	-
F	Faraday's constant (96486)	As Mol^{-1}
i_{app}	Applied current density	mA cm^{-2}
j_0	Exchange current density	mA cm^{-2}
κ_e	Ionic Conductivity of the electrolyte	mS cm^{-1}
κ_L	Ionic conductivity of the porous electrode	mS cm^{-1}
L_0	Thickness of the uncompressed felt	cm
L	Thickness of the compressed felt	cm
OCV	Open-circuit voltage	V
R	Gas constant (8.3144)	$\text{J K}^{-1} \text{Mol}^{-1}$
R_e	Single electrode resistance	$\text{m}\Omega \text{cm}^2$
R_e^Ω	Ohmic part of the single electrode resistance	$\text{m}\Omega \text{cm}^2$
R_{cc}	Contact and collector resistance	$\text{m}\Omega \text{cm}^2$
R_{DHC}	DC resistance of double-half cell	$\text{m}\Omega \text{cm}^2$
R_m	Membrane resistance	$\text{m}\Omega \text{cm}^2$
S_a	Volumetric surface area	cm^{-1}
SOC	State of charge	%
σ_S	Electronic conductivity of the solid phase (felt)	mS cm^{-1}
T	Temperature	K
y	Dimensionless exchange current	-
Z_{DHC}	(High-frequency) AC impedance of double-half cell	$\text{m}\Omega \text{cm}^2$

References

1. Skyllas-Kazacos, M.; Chakrabarti, M.H.; Hajimolana, S.A.; Mjalli, F.S.; Saleem, M. Progress in flow battery research and development. *J. Electrochem. Soc.* **2011**, *58*, R55–R79. [[CrossRef](#)]
2. Weber, A.Z.; Mench, M.M.; Meyers, J.P.; Ross, P.N.; Gostick, J.T.; Liu, Q. Redox flow batteries: A review. *J. Appl. Electrochem.* **2011**, *41*, 1137–1164. [[CrossRef](#)]
3. Soloveichik, G.L. Flow batteries: Current status and trends. *Chem. Rev.* **2015**, *115*, 11533–11558. [[CrossRef](#)] [[PubMed](#)]
4. Xu, Q.; Ji, Y.N.; Qin, L.Y.; Leung, P.K.; Qiao, F.; Li, Y.S.; Su, H.N. Evaluation of redox flow batteries goes beyond round-trip efficiency: A technical review. *J. Energy Storage* **2018**, *16*, 108–115. [[CrossRef](#)]
5. Leung, P.; Li, X.; Ponce de Leon, C.; Berlouis, L.; Low, C.T.J.; Walsh, F.C. Progress in redox flow batteries, remaining challenges and their applications in energy storage. *RSC Adv.* **2012**, *2*, 10125–10156. [[CrossRef](#)]

6. Arenas, L.F.; Ponce de León, C.; Walsh, F.C. Engineering aspects of the design, construction and performance of modular redox flow batteries for energy storage. *J. Energy Storage* **2017**, *11*, 119–153. [[CrossRef](#)]
7. Whitehead, A.H.; Rabbow, T.J.; Trampert, M.; Pokorny, P. Critical safety features of the vanadium redox flow battery. *J. Power Sources* **2017**, *351*, 1–7. [[CrossRef](#)]
8. Noack, J.; Roznyatovskaya, N.; Herr, T.; Fischer, P. The chemistry of redox-flow batteries. *Angew. Chem. Int. Ed.* **2015**, *54*, 9776–9809. [[CrossRef](#)] [[PubMed](#)]
9. Skyllas-Kazacos, M.; Grossmith, F. Efficient vanadium redox flow cell. *J. Electrochem. Soc.* **1987**, *134*, 2950–2953. [[CrossRef](#)]
10. Skyllas-Kazacos, M. Vanadium redox flow batteries. In *Encyclopedia of Electrochemical Power Sources*, 1st ed.; Elsevier Science: Amsterdam, The Netherlands, 2009; pp. 444–453.
11. Skyllas-Kazacos, M.; Cao, L.; Kazacos, M.; Kausar, N.; Mousa, A. Vanadium electrolyte studies for the vanadium redox battery—A review. *ChemSusChem* **2016**, *9*, 1–24. [[CrossRef](#)] [[PubMed](#)]
12. Roe, S.; Menictas, C.; Skyllas-Kazacos, M. A high energy density vanadium redox flow battery with 3 M vanadium electrolyte. *J. Electrochem. Soc.* **2016**, *163*, A5023–A5028. [[CrossRef](#)]
13. Schwenzer, B.; Zhang, J.; Kim, S.; Li, L.; Liu, J.; Yang, Z. Membrane development for vanadium redox flow batteries. *ChemSusChem* **2011**, *4*, 1388–1406. [[CrossRef](#)] [[PubMed](#)]
14. Prifti, H.; Parasuraman, A.; Winardi, S.; Lim, T.M.; Skyllas-Kazacos, M. Membranes for redox flow battery applications. *Membranes* **2012**, *2*, 275–306. [[CrossRef](#)] [[PubMed](#)]
15. Kim, K.J.; Park, M.S.; Kim, Y.J.; Kim, J.H.; Skyllas-Kazacos, M. A technology review of electrodes and reaction mechanisms in vanadium redox flow batteries. *J. Mater. Chem. A* **2015**, *3*, 16913–16933. [[CrossRef](#)]
16. Zheng, Q.; Li, X.; Cheng, Y.; Ning, G.; Xing, F.; Zhang, H. Development and perspective in vanadium flow battery modeling. *Appl. Energy* **2014**, *132*, 254–266. [[CrossRef](#)]
17. Xu, Q.; Zhao, T.S. Fundamental models for flow batteries. *Prog. Energy Combust. Sci.* **2015**, *49*, 40–58. [[CrossRef](#)]
18. Wei, Z.; Tseng, K.J.; Wai, N.; Lim, T.M.; Skyllas-Kazacos, M. Adaptive estimation of state of charge and capacity with online identified battery model for vanadium redox flow battery. *J. Power Sources* **2016**, *332*, 389–398. [[CrossRef](#)]
19. Shah, A.; Tangirala, R.; Singh, R.; Wills, R.G.A.; Walsh, F.C. A dynamic unit cell model for the all-vanadium flow battery. *J. Electrochem. Soc.* **2011**, *158*, A671–A677. [[CrossRef](#)]
20. Flox, C.; Rubio Garcia, J.; Skoumal, M.; Vázquez-Galván, J.; Ventosa, E.; Ramon Morante, J. Thermally stable positive electrolytes with a superior performance in all-vanadium redox flow batteries. *ChemPlusChem* **2015**, *80*, 354–358. [[CrossRef](#)]
21. Liu, H.-J.; Xu, Q.; Yan, C.-W.; Cao, Y.-Z.; Qiao, Y.-L. The effect of temperature on the electrochemical behavior of the V(IV)/V(V) couple on a graphite electrode. *Int. J. Electrochem. Sci.* **2011**, *6*, 3483–3496.
22. Langner, J.; Bruns, M.; Dixon, D.; Nefedov, A.; Wöll, C.; Scheiba, F.; Ehrenberg, H.; Roth, C.; Melke, J. Surface properties and graphitization of polyacrylonitrile based fiber electrodes affecting the negative half-cell reaction in vanadium redox flow batteries. *J. Power Sources* **2016**, *321*, 210–218. [[CrossRef](#)]
23. Fetyan, A.; El-Nagar, G.A.; Lauermann, L.; Schnucklake, M.; Schneider, J.; Roth, C. Detrimental role of hydrogen evolution and its temperature-dependent impact on the performance of vanadium redox flow batteries. *J. Energy Chem.* **2018**. [[CrossRef](#)]
24. Wei, L.; Zhao, T.S.; Xu, Q.; Zhou, X.L.; Zhang, Z.H. In-situ investigation of hydrogen evolution behavior in vanadium redox flow batteries. *Appl. Energy* **2017**, *190*, 1112–1118. [[CrossRef](#)]
25. Zhang, C.; Zhao, T.S.; Xu, Q.; An, L.; Zhao, G. Effects of operating temperature on the performance of vanadium redox flow batteries. *Appl. Energy* **2015**, *155*, 349–353. [[CrossRef](#)]
26. Xi, J.; Xiao, S.; Yu, L.; Wu, L.; Liu, L.; Xi, J.; Qiu, X. Broad temperature adaptability of vanadium redox flow battery-Part 2: Cell research. *Electrochim. Acta* **2016**, *191*, 695–704. [[CrossRef](#)]
27. Xi, J.; Jiang, B.; Yu, L.; Liu, L. Membrane evaluation for vanadium flow batteries in a temperature range of –20 to 50 °C. *J. Membr. Sci.* **2017**, *522*, 45–55. [[CrossRef](#)]
28. Yan, Y.; Skyllas-Kazacos, M.; Bao, J. Effects of battery design, environmental temperature and electrolyte flowrate on thermal behaviour of a vanadium redox flow battery in different applications. *J. Energy Storage* **2018**, *11*, 104–118. [[CrossRef](#)]
29. Schweiss, R.; Pritzl, A.; Meiser, C. Parasitic hydrogen evolution at different carbon fiber electrodes in vanadium redox flow batteries. *J. Electrochem. Soc.* **2016**, *163*, A2089–A2094. [[CrossRef](#)]

30. Bourke, A.; Miller, M.A.; Lynch, R.P.; Gao, X.; Landon, J.; Wainright, J.S.; Savinell, R.B.; Buckley, D.N. Electrode kinetics of vanadium flow batteries: Contrasting responses of VII-VIII and VIV-VV to electrochemical pretreatment. *J. Electrochem. Soc.* **2016**, *163*, A5097–A5105. [[CrossRef](#)]
31. Schweiss, R.; Meiser, C.; Goh, F.W.T. Steady-state measurements of vanadium redox-flow batteries to study particular influences of carbon felt properties. *ChemElectroChem* **2017**, *4*, 1969–1974. [[CrossRef](#)]
32. Gattrell, M.; Park, J.; MacDougall, B.; Apte, J.; McCarthy, S.; Wu, C.W. Study of the mechanism of the Vanadium 4+/5+ redox reaction in acidic solutions. *J. Electrochem. Soc.* **2004**, *151*, A123–A130. [[CrossRef](#)]
33. Melke, J.; Jakes, P.; Langner, J.; Riekehr, L.; Kunz, U.; Zhao-Karger, Z.; Nefedov, A.; Sezen, H.; Wöll, C.; Ehrenberg, H.; et al. Carbon materials for the positive electrode in all-vanadium redox flow batteries. *Carbon* **2014**, *78*, 220–230. [[CrossRef](#)]
34. Darling, R.M.; Perry, M.L. Half-cell, steady-state flow-battery experiments. *ECS Trans.* **2013**, *53*, 31–38. [[CrossRef](#)]
35. Darling, R.M.; Perry, M.L. The influence of electrode and channel configurations on flow battery performance. *J. Electrochem. Soc.* **2014**, *161*, A1381–A1387. [[CrossRef](#)]
36. Pan, J.; Huang, M.; Li, X.; Wang, S.; Li, W.; Ma, T.; Xie, X.; Ramani, V. The performance of all vanadium redox flow batteries at below-ambient temperatures. *Energy* **2016**, *107*, 784–790. [[CrossRef](#)]
37. Xiao, S.; Yu, L.; Wu, L.; Liu, L.; Qiu, X.; Xi, J. Broad temperature adaptability of vanadium redox flow battery-Part 1: Electrolyte research. *Electrochim. Acta* **2016**, *187*, 525–534. [[CrossRef](#)]
38. Chen, Q.; Gerhardt, M.R.; Aziz, M.J. Dissection of the voltage losses of an acidic quinone redox flow battery. *J. Electrochem. Soc.* **2017**, *164*, A1126–A1132. [[CrossRef](#)]
39. Newman, J.; Thomas-Alyea, K.E. *Electrochemical Systems*, 3rd ed.; Wiley & Sons: New York, NY, USA, 2004; pp. 515–534.
40. Friedl, J.; Stimming, U. Determining electron transfer kinetics at porous electrodes. *Electrochim. Acta* **2017**, *227*, 235–245. [[CrossRef](#)]
41. Fink, H.; Friedl, J.; Stimming, U. Composition of the electrode determines which half-cell's rate constant is higher in a vanadium flow battery. *J. Phys. Chem. C* **2016**, *120*, 15893–15901. [[CrossRef](#)]
42. Sun, C.-N.; Delnick, F.M.; Aaron, D.S.; Papandrew, A.B.; Mench, M.M.; Zawodzinski, T.A. Probing electrode losses in all-vanadium redox flow batteries with impedance spectroscopy. *ECS Electrochem. Lett.* **2013**, *2*, A43–A45. [[CrossRef](#)]
43. Mazúr, P.; Mrlík, J.; Beneš, J.; Pociđič, J.; Vrána, J.; Dundálek, J.; Kosek, J. Performance evaluation of thermally treated graphite felt electrodes for vanadium redox flow battery and their four-point single cell characterization. *J. Power Sources* **2018**, *380*, 105–114. [[CrossRef](#)]
44. Sun, C.-N.; Tang, Z.; Belcher, C.; Zawodzinski, T.A.; Fujimoto, C. Evaluation of Diels–Alder poly (phenylene) anion exchange membranes in all-vanadium redox flow batteries. *Electrochem. Comm.* **2014**, *43*, 63–66. [[CrossRef](#)]
45. Zhou, Y.; Yu, L.; Wang, J.; Liu, L.; Liang, F.; Xi, J. Rational use and reuse of Nafion 212 membrane in vanadium flow batteries. *RSC Adv.* **2017**, *7*, 19425–19433. [[CrossRef](#)]
46. Aaron, D.; Sun, C.-N.; Bright, M.; Papandrew, A.B.; Mench, M.M.; Zawodzinski, T.A. In situ kinetics studies in all-vanadium redox flow batteries. *ECS Electrochem. Lett.* **2013**, *2*, A29–A31. [[CrossRef](#)]
47. Davies, T.J.; Tummino, J.J. High-performance vanadium redox flow batteries with graphite felt electrodes. *J. Carbon Res.* **2018**, *4*, 8. [[CrossRef](#)]

